# Enhancement of the momentum interpolation method on non-staggered grids

J. Papageorgakopoulos, G. Arampatzis, D. Assimacopoulos* and N. C. Markatos

*Department of Chemical Engineering, National Technical University of Athens, Athens, GR-157 80, Greece*

## SUMMARY

A novel interpretation of the momentum interpolation method (MIM) is presented in this paper. A revised method using quadratic interpolating polynomials for the calculation of the cell-face velocities is proposed. The performance of the proposed method (referred to as QMIM) is examined and its application to the well-known lid-driven flow in a square enclosure problem is tested. The computed results are compared with standard reported benchmark solutions for a wide range of flow conditions. The numerical experiments show clearly the superiority of the new approach over the original MIM, in terms of numerical accuracy, rate of convergence towards the grid-independent solution, and computational efficiency. Copyright © 2000 John Wiley & Sons, Ltd.

KEY WORDS:    finite volume method; lid-driven cavity; momentum interpolation; non-staggered grid; quadratic interpolation

## 1. INTRODUCTION

In recent years, finite volume methods have become very popular for solving the incompressible Navier–Stokes equations. When primitive variables (e.g. velocities and pressure) are used, special treatment is required in the solution algorithm and the grid system used. The reason stems from the fact that pressure does not have its own governing equation. The continuity equation, having no explicit link to the pressure, is just an additional constraint on the velocity field that must be satisfied together with the momentum equations, and it is an appropriate manipulation of that constraint that leads to an equation for pressure correction [1].

The marker-and-cell (MAC) type staggered grid arrangement [1] (Figure 1(a)) of velocities and scalar variables, first proposed by Harlow and Welch [2], has been widely used with great success [3–6]. The main disadvantages of such an arrangement are the geometrical complexity (due to the different sets of grids used for different variables), the discretization complexity of the boundary conditions, and the difficulty of implementation to non-orthogonal curvilinear grids [7] and multigrid solution methods.

* Correspondence to: Department of Chemical Engineering, National Technical University of Athens, 9 Heroon Polytechnion Street, Zografou Campus, Athens, GR-157 80, Greece.
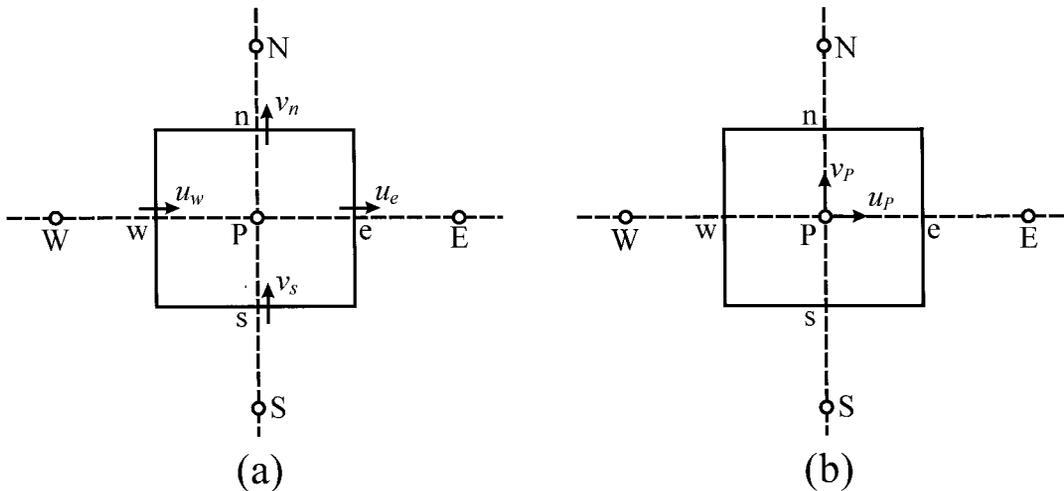
Figure 1. Typical control volume and velocities arrangement in (a) staggered and (b) non-staggered grid.

The use of a non-staggered grid arrangement, which stores all the variables at the same physical location and employs only one set of control volumes (Figure 1(b)), reduces the geometrical complexity and shortens the long computational time needed in the conventional staggered methods. Though practically attractive, this arrangement has been shown to produce non-physical oscillations in the pressure field [1]. This behavior occurs when central differencing is used to represent both the pressure gradient terms in the momentum equations and the cell-face velocities in the continuity equation. It is then obvious that the momentum equations depend on pressures at alternate nodes and the continuity equation on velocities at alternate nodes and not on adjacent ones. This behavior is called velocity–pressure decoupling [8].

A remedy to the above problem is the momentum interpolation method (MIM), first proposed by Rhie and Chow [9]. In this approach, the cell-face velocities in the continuity equation are evaluated by linearly interpolating the discretized momentum equations for the neighboring cell-centered velocities. This practice results in a strong velocity–pressure coupling. The pressure gradient terms, appearing in the momentum equations, are still represented by central difference approximation.

Subsequent work by Peric [7] refined the original method further. Majumdar [10] and Miller and Schmidt [11] have removed the problem of underrelaxation parameter dependency of the results, observed in Rhie and Chow's formula. Previous authors have reported performance comparisons between the staggered and non-staggered grid arrangements [11–16].

In this paper, a new interpretation of the MIM is provided. According to this interpretation, the cell-face velocities used in the continuity equation consist of two terms. A linear interpolation part of the neighboring pseudo-velocities (velocities that contain no pressure effects) and a correction part that represents the contribution of the pressure gradient term on the staggered control volume. Based on this interpretation, it is shown that enhancements of

the original method can be derived by using higher-order interpolating functions for the evaluation of the cell-face pseudo-velocities. Subsequently, a new formula based on quadratic interpolating polynomials is proposed. The same quadratic formula is also used for the representation of the pressure gradient terms. This results in a method of a greater formal accuracy that, at the same time, retains the basic characteristics of the momentum interpolation. This method is called the quadratic momentum interpolation method (QMIM).

In the following section, the equations to be solved are presented. The exposition will be given for a two-dimensional field in order to preserve clarity of presentation. Extension to three dimensions is simple and straightforward. The solution of these equations with the MIM and its new interpretation is then given. The revised version of the method based on quadratic interpolation functions is derived and its implementation in the SIMPLEC algorithm [4] is described. Finally, in Section 3, the performance of the new scheme is examined through computations of the lid-driven square cavity problem. Conclusions are summarized in Section 4.

## 2. MATHEMATICAL FORMULATION

### 2.1. *The problem*

The governing conservation equations for steady, two-dimensional, incompressible flows in Cartesian or polar–cylindrical co-ordinates, with reference to Table I, can be written in the form

$$\frac{\partial}{\partial x}(\rho u \varphi) + \frac{1}{r^a}\frac{\partial}{\partial y}(r^a \rho v \varphi) = \frac{\partial}{\partial x}\left(\Gamma \frac{\partial \varphi}{\partial x}\right) + \frac{1}{r^a}\frac{\partial}{\partial y}\left(r^a \Gamma \frac{\partial \varphi}{\partial y}\right) + S, \tag{1}$$

where $\Gamma$ is the effective diffusion coefficient and $S$ is the source term [1].

The discretization of the transport equations is performed using the finite volume approach [1]. The computational domain is divided into a number of quadrilateral control volumes and

Table I. Expressions of the effective diffusion coefficient $\Gamma$ and source the term $S$ in the momentum and continuity equations[a]

| Equation | $\varphi$ | $\Gamma$ | $S$ |
|---|---|---|---|
| $x$-Momentum | $u$ | $\mu$ | $-\dfrac{\partial P}{\partial x} + \dfrac{\partial}{\partial x}\left(\mu \dfrac{\partial u}{\partial x}\right) + \dfrac{1}{r^a}\dfrac{\partial}{\partial y}\left(r^a \mu \dfrac{\partial v}{\partial x}\right)$ |
| $y$-Momentum | $v$ | $\mu$ | $-\dfrac{\partial P}{\partial y} + \dfrac{\partial}{\partial x}\left(\mu \dfrac{\partial u}{\partial y}\right) + \dfrac{1}{r^a}\dfrac{\partial}{\partial y}\left(r^a \mu \dfrac{\partial v}{\partial y}\right) - \dfrac{a2\mu v}{r^2}$ |
| Continuity | $1$ | $0$ | $0$ |

[a] $a = 1$ for cylindrical and $a = 0$ for Cartesian co-ordinates.

all variables are stored at the geometric center of each control volume (Figure 1(b)). Integration of Equation (1) over the control volume surrounding node $P$ yields an algebraic equation representing the balance of fluxes. The resulting algebraic equations for the $u$ velocity component at node $P$ have the form

$$a_P|_P u_P = \sum_k a_k u_k|_P + b_P - A_P^x(P_e - P_w). \tag{2}$$

The coefficients $a_i$, representing the convection and diffusion effects, depend on the discretization scheme used and the index $k$ usually runs over the four neighboring nodes of $P$ (E, W, N and S in Figure 1(b)). The $b_P$ stands for the constant part of the discretized source term, which does not include the pressure gradient and $A_P^x$ is a representative cross-sectional area at node $P$. The last term in the above equation represents the $x$-direction pressure driving force acting on the control volume. A similar equation can be obtained for the $v_P$ velocity component. The discretized form of the continuity equation is given by

$$\rho_e u_e A_e^x - \rho_w u_w A_w^x + \rho_n v_n A_n^y - \rho_s v_s A_s^y = 0. \tag{3}$$

Special attention should be given to the evaluation of cell-face velocities appearing in the continuity equation (3), and the cell-face pressure values appearing in the momentum equations (2), in order to avoid the velocity–pressure decoupling problem [1,8] and the subsequent non-physical oscillations in the pressure field.

## 2.2. Momentum interpolation method

Rhie and Chow [9] suggested the use of the same discretization equation for the cell-face velocities as for the nodal ones where all terms, with the exception of the pressure gradient, are obtained through linear interpolation of the corresponding terms in the equations for the neighboring cell-centered velocities. The pressure gradient term is not interpolated but replaced by the difference of pressure at the nodes between which the cell-face lies. This approach is known as the MIM. In a general, two-dimensional, non-uniform grid, the east face velocity, for example, is defined as follows:

$$u_e = \frac{\sum_k a_k u_k|_e}{a_P|_e} + \frac{b_e}{a_P|_e} - \frac{A_e^x}{a_P|_e}(P_E - P_P), \tag{4}$$

where

$$\frac{\sum_k a_k u_k|_e}{a_P|_e} = f_P^x \frac{\sum_k a_k u_k|_E}{a_P|_E} + (1 - f_P^x)\frac{\sum_k a_k u_k|_P}{a_P|_P}, \tag{5}$$

$$\frac{b_e}{a_P|_e} = f_P^x \frac{b_e}{a_P|_E} + (1 - f_P^x) \frac{b_P}{a_P|_P}, \tag{6}$$

$$\frac{1}{a_P|_e} = f_P^x \frac{1}{a_P|_E} + (1 - f_P^x) \frac{1}{a_P|_P}, \tag{7}$$

and $f_P^x$ is the $x$-direction linear interpolation factor, defined in terms of distances between nodes as

$$f_P^x = \frac{\overline{P_e}}{\overline{P_E}} = \frac{x_e - x_P}{x_E - x_P}. \tag{8}$$

The last term in Equation (4) represents the net pressure driving force acting on the 'staggered' control volume surrounding the east face.

By substituting Equations (5) and (6) into Equation (4) and rearranging, the cell-face velocity can be expressed explicitly in terms of the known nodal velocities

$$u_e = f_P^x u_E + (1 - f_P^x) u_P + f_P^x \frac{A_E^x}{a_P|_E} (P_{ee} - P_e) + (1 - f_P^x) \frac{A_P^x}{a_P|_P} (P_e - P_w) - \frac{A_e^x}{a_P|_e} (P_E - P_P). \tag{9}$$

Similar expressions can be obtained for the other cell-face velocities $u_w$, $v_n$, $v_s$.

### 2.3. The new interpretation

The above expression (9) can be recast in a more compact format, which provides simplicity and clarity. First, the momentum equation (2) giving the nodal velocity $u_P$ is rewritten in a more convenient form,

$$u_P = \hat{u}_P + \bar{u}_P, \tag{10}$$

where $\hat{u}_P$ is a pseudo-velocity [1] composed of the neighboring velocities and containing no pressure terms,

$$\hat{u}_P = \frac{\sum_k a_k u_k|_P}{a_P|_P} + \frac{b_P}{a_P|_P}, \tag{11}$$

and $\bar{u}_P$ represents the contribution of pressure to the actual value of velocity,

$$\bar{u}_P = -\frac{A_P^x}{a_P|_P} (P_e - P_w). \tag{12}$$

Using the above splitting formulation, Equation (4) can be recast into the following form:

$$u_e = \hat{u}_e + \bar{u}_e, \tag{13}$$

where

$$\hat{u}_{\mathrm{e}} = f_P^x \hat{u}_{\mathrm{E}} + (1 - f_P^x) \hat{u}_P \tag{14}$$

and

$$\bar{u}_{\mathrm{e}} = -\frac{A_{\mathrm{e}}^x}{a_P|_{\mathrm{e}}} (P_{\mathrm{E}} - P_P). \tag{15}$$

As can be seen, the expression giving $u_{\mathrm{e}}$ (13) is made up of two parts. The first part, representing the cell-face pseudo-velocity, is approximated by a linear interpolation of the neighboring cell-centered pseudo-velocities. The second part stands for the contribution of pressure and is evaluated by the pressure difference acting on the 'staggered' control volume surrounding $u_{\mathrm{e}}$. The above observation is diagrammatically depicted in Figure 2. In the same figure, the linear interpolation of the two cell-centered velocities $u_{\mathrm{me}}$ is also portrayed. The difference between this velocity and the one obtained by momentum interpolation, given by the last three terms of the right-hand side of Equation (9), is responsible for removing the velocity–pressure decoupling.

Equation (13) has a form similar to the momentum equations giving the cell-face velocities in the conventional staggered grid arrangement. In the staggered grid method, the cell-face pseudo-velocities are evaluated using the algebraic coefficients calculated on the staggered control volumes. In the Rhie and Chow momentum interpolation practice, these pseudo-velocities are evaluated explicitly, by linear interpolation of the cell-centered pseudo-velocities. However, in the staggered grid method, linear interpolation is applied for the evaluation of



Figure 2. Principle of the linear and momentum interpolation for evaluation of cell-face velocities.

convective velocities used in the coefficients of momentum equations. Many researchers [11,14–16] have shown that SIMPLE-like algorithms on non-staggered grids, supplied with the momentum interpolation practice, provide exactly the same results and the same convergence behavior when compared with SIMPLE-like algorithms on staggered grids. The need for more accurate results, especially on coarse grids, makes a further effort in improving the MIM necessary, i.e. in the use of a more accurate interpolation practice for the evaluation of the cell-face pseudo-velocities.

### 2.4. Quadratic momentum interpolation

An interpolation formula that has been shown to offer high accuracy in the field of computational fluid dynamics (CFD) is quadratic polynomial interpolation, used in the development of the QUICK differencing scheme [17]. The general form of the quadratic interpolation formula has been presented by Arambatzis *et al.* [18] in their formulation of the QUICK scheme. According to this formulation, the formulae giving the general transport quantity $\varphi$ at the east and north cell-faces for a two-dimensional flow have the following form:

$$\varphi_{e} = Q_{e}(\varphi)$$

$$= \begin{cases} \varphi_P + QAE_P(\varphi_P - \varphi_{\mathrm{W}}) + QBE_P(\varphi_{\mathrm{E}} - \varphi_P) + QC_P(\varphi_{\mathrm{S}} - \varphi_P) + QD_P(\varphi_{\mathrm{N}} - \varphi_P) & u_{\mathrm{e}} \geq 0 \\ \varphi_{\mathrm{E}} + QAW_{\mathrm{E}}(\varphi_P - \varphi_{\mathrm{E}}) + QBW_{\mathrm{E}}(\varphi_{\mathrm{E}} - \varphi_{\mathrm{EE}}) + QC_{\mathrm{E}}(\varphi_{\mathrm{SE}} - \varphi_{\mathrm{E}}) + QD_{\mathrm{E}}(\varphi_{\mathrm{NE}} - \varphi_{\mathrm{E}}) & u_{\mathrm{e}} < 0 \end{cases},$$

(16)

$$\varphi_{n} = Q_{n}(\varphi)$$

$$= \begin{cases} \varphi_P + QCN_P(\varphi_P - \varphi_{\mathrm{S}}) + QDN_P(\varphi_{\mathrm{N}} - \varphi_P) + QA_P(\varphi_{\mathrm{W}} - \varphi_P) + QB_P(\varphi_{\mathrm{E}} - \varphi_P) & v_{\mathrm{n}} \geq 0 \\ \varphi_{\mathrm{N}} + QCS_{\mathrm{N}}(\varphi_P - \varphi_{\mathrm{N}}) + QDS_{\mathrm{N}}(\varphi_{\mathrm{N}} - \varphi_{\mathrm{NN}}) + QA_{\mathrm{N}}(\varphi_{\mathrm{NW}} - \varphi_{\mathrm{N}}) + QB_{\mathrm{N}}(\varphi_{\mathrm{NE}} - \varphi_{\mathrm{N}}) & v_{\mathrm{n}} < 0 \end{cases},$$

(17)

where the coefficients $QAE_p$, $QBE_P$, etc., are functions of the distances between nodes and are given in Appendix A. The above formulae, representing the face averages of the quantity $\varphi$, are derived by fitting a parabola to the nodal values and integrating along the cell-faces (see Arampatzis *et al.* [18]).

Using the above formulae for the evaluation of cell-face pseudo-velocities, the expressions giving the east face velocity can be written as

$$u_{\mathrm{e}} = Q_{\mathrm{e}}(\hat{u}) + \bar{u}_{\mathrm{e}}.$$

(18)

Figure 3 depicts the principle of the expression (18), in a one-dimensional flow. As can be seen, the cell-face pseudo-velocity is obtained by fitting a parabola to the values of pseudo-velocity at three consecutive nodes; the two neighboring nodes plus the adjacent node on the upstream side.
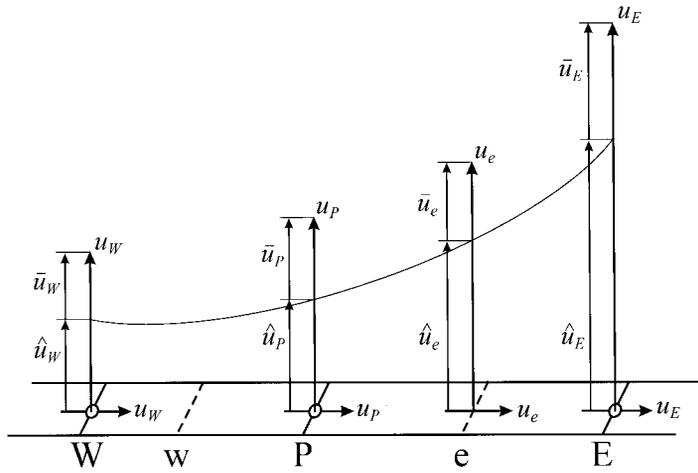
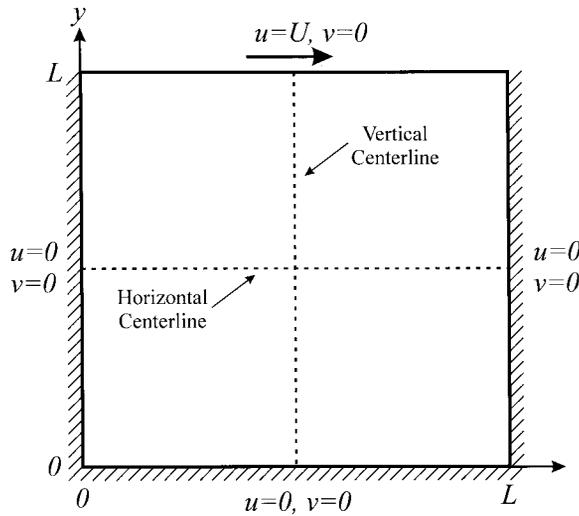Figure 3. Principle of quadratic momentum interpolation for evaluation of cell-face velocities.



Figure 4. Lid-driven cavity configuration and boundary conditions.

Equation (18) can be expressed in the following computationally efficient form, using the cell-centered momentum equations (11):

$$u_e = Q_e(u) + \bar{u}_e - Q_e(\bar{u}). \tag{19}$$

This expression does not contain pseudo-velocities but velocity and pressure values, and can be used immediately to compute $u_{\mathrm{e}}^n$, requiring no extra storage.

A similar expression can be obtained for the north face velocity

$$v_{\mathrm{n}} = Q_{\mathrm{n}}(v) + \bar{v}_{\mathrm{n}} - Q_{\mathrm{n}}(\bar{v}). \qquad (20)$$

The proposed interpolation is more appropriate when used in combination with the QUICK differencing scheme, where the convected cell-face velocities are approximated to third-order by formulae (16) and (17), setting $\varphi = u$ or $v$. The Rhie and Chow momentum interpolation of the convecting cell-face velocities is of only second-order (the order of linear interpolation, see Miller and Schmidt [11]). In the new quadratic momentum interpolation scheme, the convecting cell-face velocities are approximated to third-order by formulae (19) and (2), giving an overall third-order accuracy to the finite difference equations.

## 2.5. Effect of relaxation factor

When underrelaxation is incorporated to update the cell center velocities, $a_P|_P$ in Equation (2) is changed to $a_P|_P/\omega^u$. As explained by Majumdar [10], this gives an interpolation method that depends on the relaxation factor $\omega^u$. This problem can be resolved by employing an explicit underrelaxation in Equation (19) as
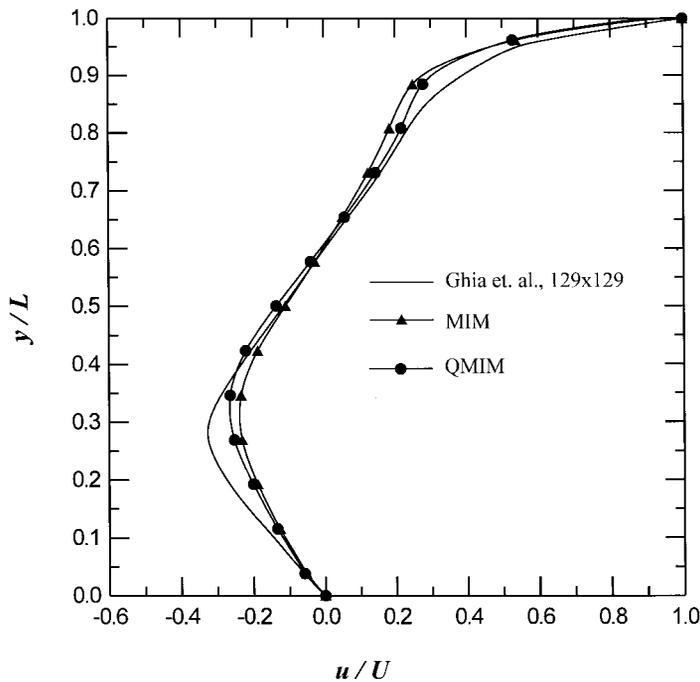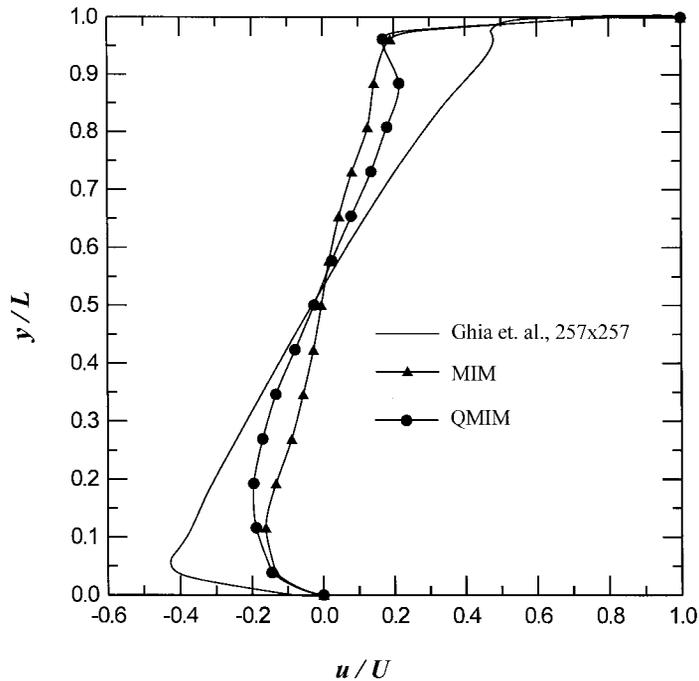


Figure 5. Horizontal velocity profile along cavity centerline, $Re = 400$.
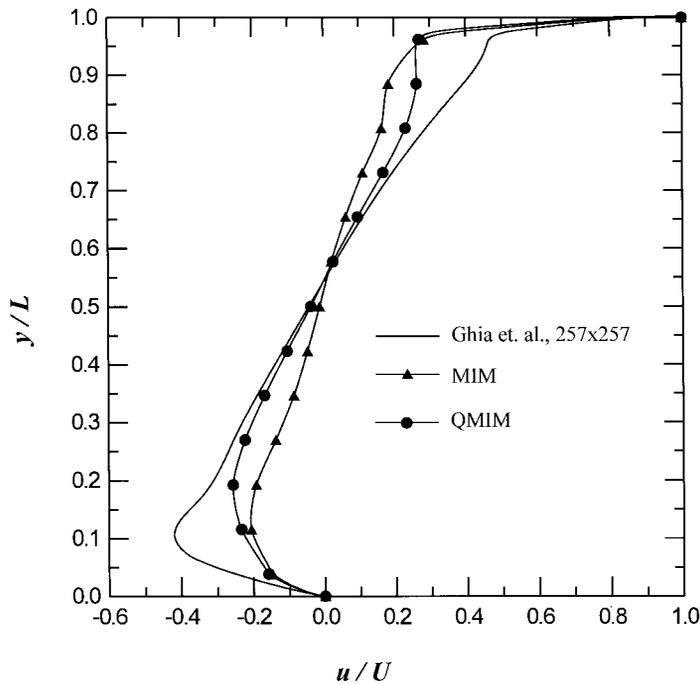
Figure 6. Horizontal velocity profile along cavity centerline, $Re = 3200$.

$$u_e = \omega^u[Q_e(u) + \bar{u} - Q_e(\bar{u})] + (1 - \omega^u)u_e^{n-1}, \tag{21}$$

where the superscript $n - 1$ refers to the previous iteration level. The above expression is independent of the relaxation factor and it is more efficient than the one proposed by Majumdar [10], which requires the storage of the cell-centered velocities at the previous iteration level. Similarly, Equation (20) takes the form

$$v_n = \omega^v[Q_n(v) + \bar{v}_n - Q_n(\bar{v})] + (1 - \omega^v)v_n^{n-1}. \tag{22}$$

### 2.6. Evaluation of cell-face pressures

In order to preserve overall consistency in an algorithm using the quadratic momentum interpolation practice, it is reasonable to adopt the same interpolation method when calculating the pressure values at the cell faces. These values are needed for the evaluation of the correction part of cell-face velocities according to the above interpolation practice, and also for the calculation of the pressure gradient source term in the momentum equations. The interpolation equations used are (16) and (17), where $\varphi = P$.

## 2.7. Implementation of QMIM in SIMPLEC

In the present study, the coupling between the continuity and the momentum equation is treated by the SIMPLEC [4] algorithm. In the first step of SIMPLEC, the pressure field from a previous iteration $P^*$ determines a tentative velocity field $u^*$. To get a converged solution, these starred fields have to be corrected by pressure and velocity corrections $P'$, $u'$. According to the SIMPLEC algorithm, the pressure and velocity corrections are related through the relation

$$u'_P = -\omega^u A_P^x d_P^u (P'_e - P'_w), \tag{23}$$

where

$$d_P^u = \frac{1}{(1 - \omega^u)a_P|_P - \omega^u S_P|_P}. \tag{24}$$

The continuity equation, however, requires the velocities at the cell faces only and not at the cell centers. Following the principle of SIMPLEC, one may obtain the expression connecting the pressure and cell-face velocity corrections



Figure 7. Horizontal velocity profile along cavity centerline, $Re = 10\,000$.
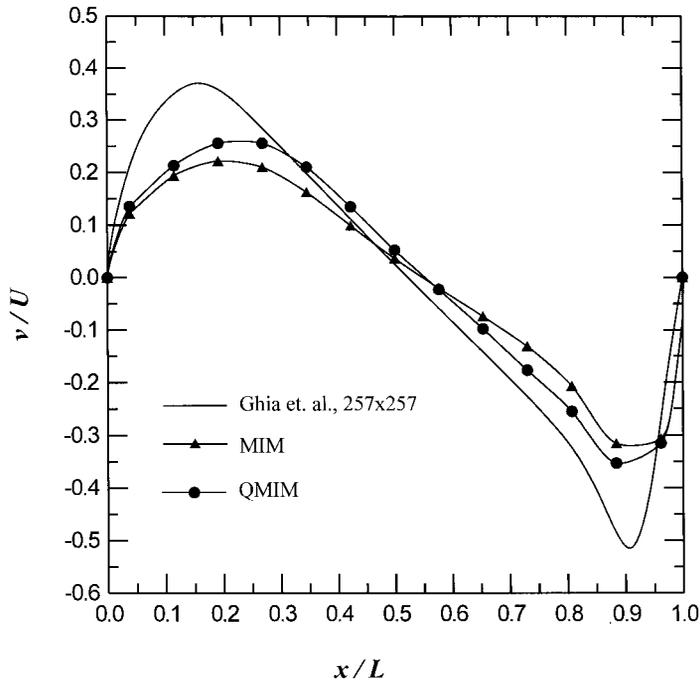
Figure 8. Vertical velocity profile along cavity centerline, $Re = 1000$.

$$u'_\mathrm{e} = -\omega^u A_\mathrm{e}^x d_\mathrm{e}^u (P'_\mathrm{E} - P'_P), \tag{25}$$

where the $d_\mathrm{e}^u$ is given by the quadratic interpolation of the neighboring nodal ones,

$$d_\mathrm{e}^u = Q_\mathrm{e}(d^u). \tag{26}$$

In a similar manner, analogous expressions can be derived for all the cell-face velocities appearing in the continuity equation. Inserting these expressions into the continuity equation (3), the pressure correction equation is obtained as

$$a_P P_P = \sum_k a_k P_P + b_P, \tag{27}$$

where

$$a_\mathrm{E} = \omega^u \rho_\mathrm{e} A_\mathrm{e}^x A_\mathrm{e}^x d_\mathrm{e}^u, \qquad a_\mathrm{N} = \omega^v \rho_\mathrm{n} A_\mathrm{n}^y A_\mathrm{n}^y d_\mathrm{n}^v, \qquad a_P = \sum_k a_k, \tag{28}$$

$$b_P = -\rho_e u_e^* A_e^x + \rho_w u_w^* A_w^x - \rho_n v_n^* A_n^y + \rho_s v_s^* A_s^y. \tag{29}$$

The solution algorithm for the QMIM can be stated as follows:

1. Start with guessed values for velocity and pressure.
2. Solve the momentum equations to obtain the starred nodal velocities.
3. Calculate the starred cell-face velocities using Equations (21) and (22).
4. Solve the pressure correction equation.
5. Correct the pressure.
6. Correct the nodal velocities using Equation (23).
7. Correct the cell-face velocities using Equation (25).
8. Repeat steps (2)–(7) until convergence is reached.

## 3. APPLICATION TO A TEST PROBLEM

### 3.1. *The test problem*

The proposed QMIM is applied to the well-known lid-driven square cavity problem, in order to validate the calculation procedure as well as to assess its performance relative to Rhie and
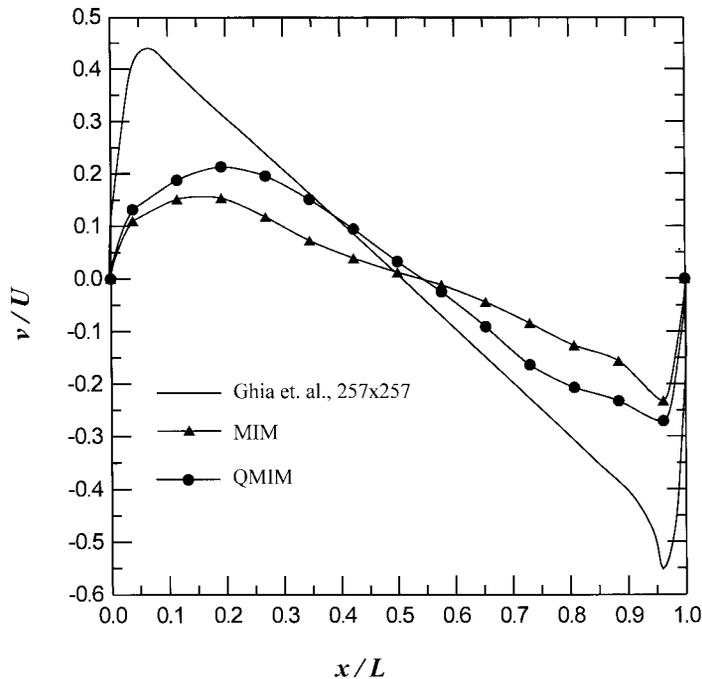


Figure 9. Vertical velocity profile along cavity centerline, $Re = 7500$.
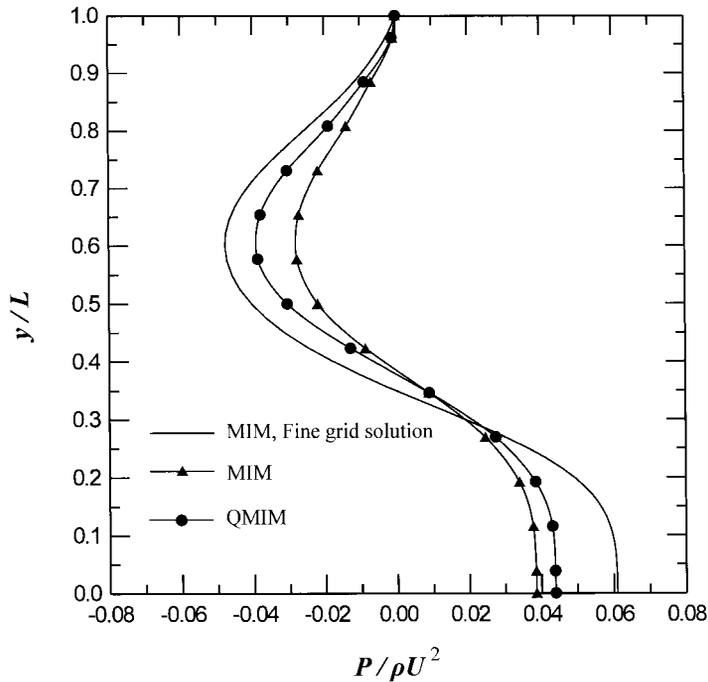
Figure 10. Pressure distribution along cavity centerline, $Re = 400$.

Chow's MIM. Because of its geometric simplicity and strongly elliptical character, this case has been served as a standard benchmark problem for the evaluation of new algorithms. Ghia *et al.* [19] reported extensive solutions based on a vorticity–streamfunction formulation of the flow equations and using a second-order differencing scheme and uniform fine-grid structures of $129 \times 129$ and $257 \times 257$ nodes.

Figure 4 shows the flow geometry and the boundary conditions used. The problem is solved for Reynolds numbers ranging from 400 to 10 000. The Reynolds number is defined by $Re = \rho UL/\mu$, where $L$ is the length of the cavity and $U$ is the velocity of the sliding wall. The QUICK differencing scheme of Leonard [17], as presented in Reference [18], is used for the discretization of the convective terms and the algebraic equations are solved by the strongly implicit procedure (SIP) [20]. Each calculation was terminated when the sum of absolute residuals for the continuity, $u$-momentum and $v$-momentum equations became less then $10^{-5}$. The residual is defined as

$$r^n = A\varphi^n - B, \tag{30}$$

where $A$ represents the finite difference coefficient matrix and $B$ represents the source term for the finite difference equations.

## 3.2. The effect of Reynolds number

Figures 5–7 show the comparison of the horizontal velocity profiles along the vertical cavity centerline ($x/L = 0.5$) for Reynolds numbers 400, 3200 and 10000. The results are non-dimensionalized using the velocity of the sliding wall $U$. Each figure provides a comparison between the original MIM and the QMIM. Also, the results calculated by Ghia *et al.* [19] are shown. All the results presented in this section are obtained on a coarse, uniformly spaced grid consisting of $15 \times 15$ nodes (13 internal control volumes in each direction).

The comparisons clearly show the superior accuracy of the QMIM. The profiles plotted in Figure 5, for $Re = 400$, show that the results obtained by the QMIM are in closer agreement with the benchmark solution for all computational nodes. As the Reynolds number increases (Figures 6 and 7), the differences between the two methods with respect to the benchmark results become more significant. This indicates that, at higher Reynolds numbers, the approximations adopted for the evaluation of cell-face pseudo-velocities and the cell-face pressures have significantly more influence on the accuracy of the final solution. This is the desirable behavior of the new method making it suitable for high-Reynolds numbers simulations.

Profiles of the non-dimensional vertical velocity ($v/U$) along the horizontal cavity centerline ($y/L = 0.5$) are shown in Figures 8 and 9 for Reynolds numbers 1000 and 7500. The same observations as before can be made.
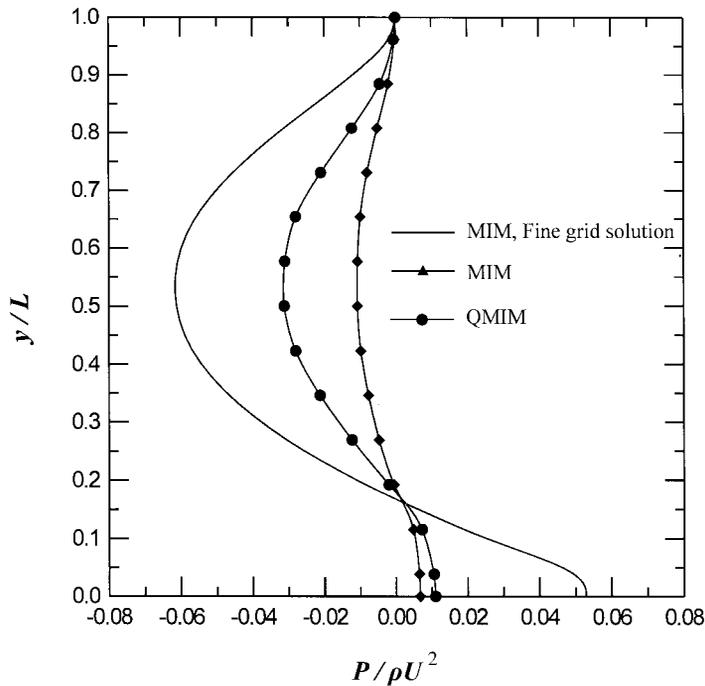


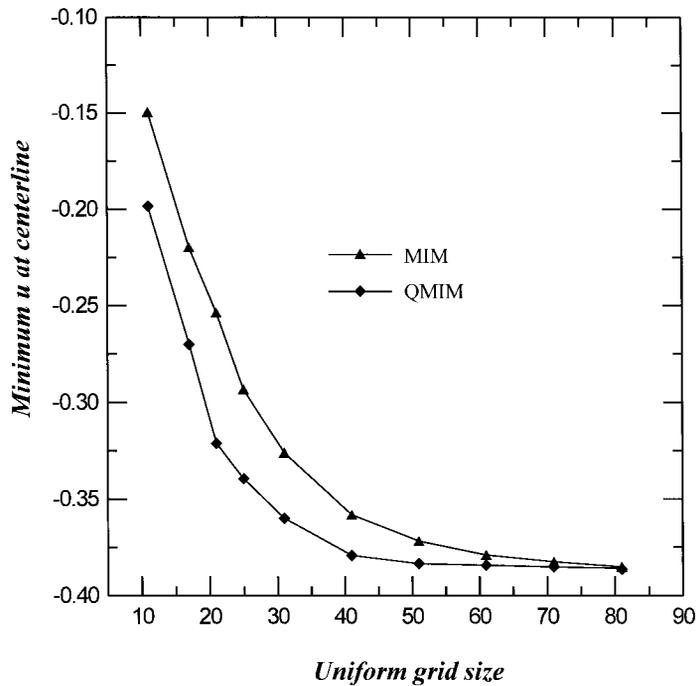Figure 11. Pressure distribution along cavity centerline, $Re = 7500$.

Figure 12. Variation of minimum horizontal velocity along cavity centerline as a function of grid refinement, $Re = 1000$.

Figures 10 and 11 show the pressure profiles along the vertical centerline for Reynolds numbers 5000 and 7500, obtained by the MIM and QMIM methods. Ghia *et al.* did not reported benchmark solutions for pressure. For this reason, the results are compared with the solution obtained on a fine grid ($155 \times 155$ nodes) using the MIM method. All the pressure values are non-dimensionalized according to the relation $p^* = (P - P_{y=L})/\rho U^2$.

### 3.3. The effect of grid refinement

A study of the influence of grid refinement on the calculated results is presented in Figures 12 and 13. The value of the minimum predicted horizontal velocity at the vertical centerline, plotted as a function of grid size for Reynolds numbers 1000 and 5000, is shown. It is clear that the QMIM converges faster to the grid-independent solution for both cases. The results for QMIM with $52 \times 52$ nodes are accurate enough to be regarded as grid-independent, even at the highest Reynolds number used. The results obtained by the MIM method, for the same grid size, are still poor. To achieve the grid-independent solution, the MIM method requires a grid with more than $72 \times 72$ nodes. It is obvious that considerable saving in computational time and storage can be made using the QMIM instead of the original Rhie and Chow method.

A comparison of the two methods, in terms of the computational cost to a given level of accuracy, is presented in Figure 14 for $Re = 1000$. The horizontal axis represents the accuracy of the results, as

$$\text{Accurancy (per cent)} = \left(1 - \frac{u_G - u_c}{u_G}\right) \times 100, \tag{31}$$

where $u_c$ is the minimum predicted horizontal velocity at the vertical centerline and $u_G$ is the one predicted by Ghia et al. [19]. The vertical axis represents the overall computational cost (CPU time and storage requirements) as

$$\text{Computational cost (per cent)} = \frac{t}{t_{\max}} \times \frac{N}{N_{\max}} \times 100, \tag{32}$$

where $t$ and $N$ are the CPU time and the total grid nodes required by the run, where $t_{\max}$ and $N_{\max}$ are the ones required by the most expensive run. The curve corresponding to the QMIM is always below the one corresponding to the MIM. This clearly shows that the new method
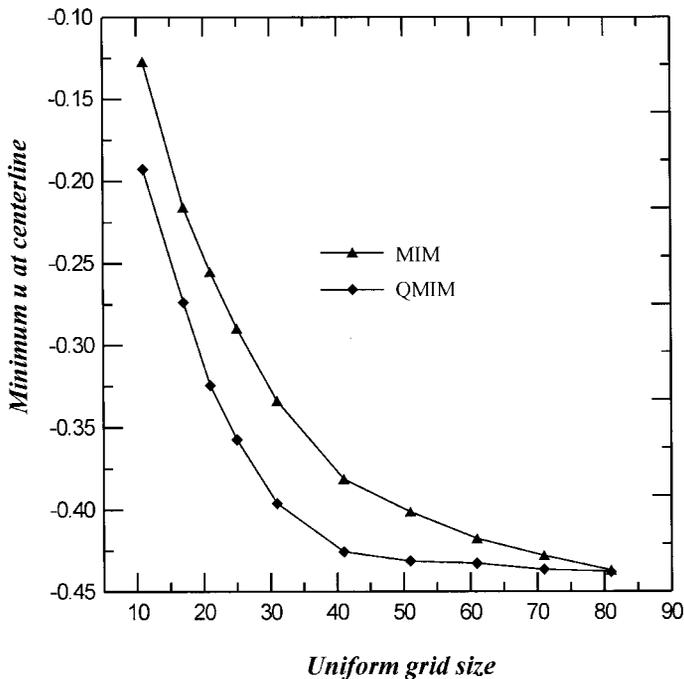


Figure 13. Variation of minimum horizontal velocity along cavity centerline as a function of grid refinement, $Re = 5000$.
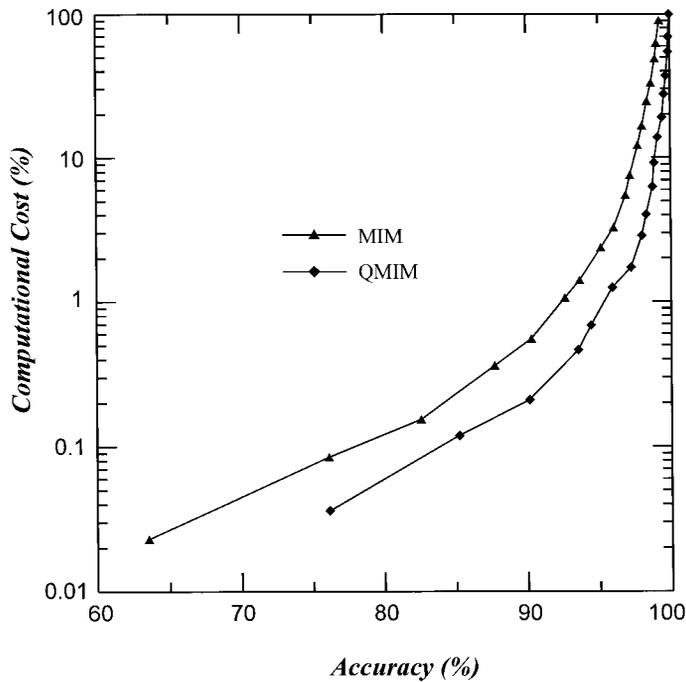
Figure 14. Computational efficiency diagram (accuracy versus cost), *Re* = 1000.

requires less computer resources in order to achieve a given level of accuracy. The computational costs of the MIM and QMIM, for a level of accuracy equal to 99 per cent, are 54 and 12 per cent respectively, and for this accuracy, the QMIM is 4.5 times more cost-effective.

Finally, Figure 15 portrays a comparison of the results obtained by the QMIM on the finest grid (101 × 101 nodes) with the results of Ghia *et al.* (257 × 257 nodes) at *Re* = 1000. The two curves are almost identical, confirming the behavior of the QMIM on fine grids when severe under or overshooting problems are likely to arise.

## 4. CONCLUSIONS

In this paper it is shown that the original MIM can be presented in a more convenient way with a more compact formulation. The new interpretation was based on the observation that the discretized momentum equations for the cell-face velocities are composed of two parts. A pseudo-velocity part calculated by the interpolation of the neighboring pseudo-velocities, and a pressure driving force term on the 'staggered' control volume. Further, a new method (the QMIM) was proposed, which uses quadratic interpolation formulae to determine the cell-face pseudo-velocities. New compact and computationally efficient expressions, containing no
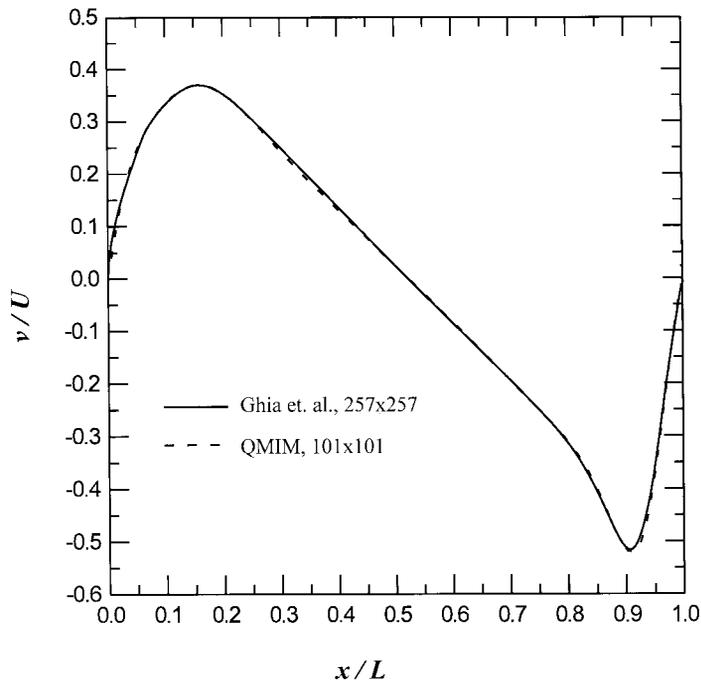
Figure 15. Comparison of the QMIM fine grid solution with Ghia *et al.*'s results, *Re* = 1000.

pseudo-velocities have been derived in order to be used in computer codes. Special attention has been given to the implementation of underrelaxation practice in the new method. More computationally convenient expressions, requiring no extra storage, have been derived. Cell-face pressures were also calculated by the same interpolation formulae in order to maintain overall consistency in the new method. Finally, the implementation of QMIM in the SIM-PLEC algorithm has been described.

The proposed QMIM has been found to give more accurate results than the original MIM. The difference between the two methods increases as the Reynolds number increases in the lid-driven cavity benchmark problem. A grid refinement study has clearly shown the superiority of the QMIM relating to computational time and storage requirements.

## APPENDIX A. COEFFICIENTS OF QUADRATIC INTERPOLATION FORMULAE

The coefficients appearing in Equations (16) and (17) are defined in terms of distances between nodes. For a general non-uniform grid, Figure 16, these coefficients are given by [18]
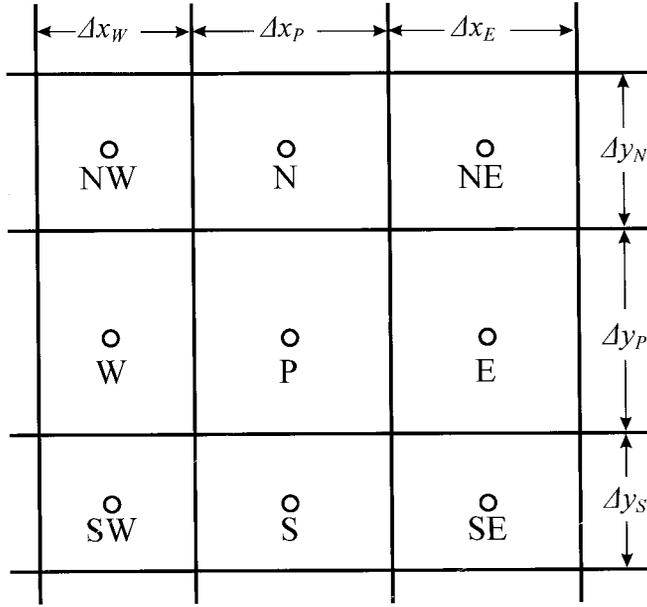
Figure 16. A typical grid, labelling scheme and distances between nodes.

$$QA_P = \frac{\Delta x_P^2}{3(\Delta x_P + \Delta x_W)(\Delta x_W + 2\Delta x_P + \Delta x_E)}, \tag{33}$$

$$QB_P = \frac{\Delta x_P^2}{3(\Delta x_P + \Delta x_E)(\Delta x_W + 2\Delta x_P + \Delta x_E)}, \tag{34}$$

$$QC_P = \frac{\Delta y_P^2}{3(\Delta y_P + \Delta y_S)(\Delta y_S + 2\Delta y_P + \Delta y_N)}, \tag{35}$$

$$QD_P = \frac{\Delta y_P^2}{3(\Delta y_P + \Delta y_N)(\Delta y_S + 2\Delta y_P + \Delta y_N)}, \tag{36}$$

$$QAE_P = \frac{\Delta x_P \Delta x_E}{3(\Delta x_P + \Delta x_W)(\Delta x_W + 2\Delta x_P + \Delta x_E)}, \tag{37}$$

$$QBE_P = \frac{2\Delta x_P^2 + \Delta x_P \Delta x_W}{(\Delta x_P + \Delta x_E)(\Delta x_W + 2\Delta x_P + \Delta x_E)}, \tag{38}$$

$$QAW_P = \frac{2\Delta x_P^2 + \Delta x_P \Delta x_E}{(\Delta x_P + \Delta x_W)(\Delta x_W + 2\Delta x_P + \Delta x_E)}, \tag{39}$$

$$QBW_P = \frac{\Delta x_P \Delta x_{\mathrm{W}}}{(\Delta x_P + \Delta x_{\mathrm{E}})(\Delta x_{\mathrm{W}} + 2\Delta x_P + \Delta x_{\mathrm{E}})},$$

(40)

$$QCN_P = \frac{\Delta y_P \Delta y_{\mathrm{N}}}{(\Delta y_P + \Delta y_{\mathrm{S}})(\Delta y_{\mathrm{S}} + 2\Delta y_P + \Delta y_{\mathrm{N}})},$$

(41)

$$QDN_P = \frac{2\Delta y_P^2 + \Delta y_P \Delta y_{\mathrm{S}}}{(\Delta y_P + \Delta y_{\mathrm{N}})(\Delta y_{\mathrm{S}} + 2\Delta y_P + \Delta y_{\mathrm{N}})},$$

(42)

$$QCS_P = \frac{2\Delta y_P^2 + \Delta y_P \Delta y_{\mathrm{N}}}{(\Delta y_P + \Delta y_{\mathrm{S}})(\Delta y_{\mathrm{S}} + 2\Delta y_P + \Delta y_{\mathrm{N}})},$$

(43)

$$QDS_P = \frac{\Delta y_P \Delta y_{\mathrm{S}}}{(\Delta y_P + \Delta y_{\mathrm{S}})(\Delta y_{\mathrm{S}} + 2\Delta y_P + \Delta y_{\mathrm{N}})}.$$

(44)

## REFERENCES

1. Patankar SV. *Numerical Heat Transfer and Fluid Flow*. Hemisphere: New York, 1980.
2. Harlow FH, Welch JE. Numerical calculation of time-dependent viscous incompressible flow of fluid with free surface. *The Physics of Fluids* 1965; **8**: 2182–2189.
3. Patankar SV, Spalding DB. A calculation procedure for heat, mass and momentum transfer in three-dimensional parabolic flows. *International Journal for Heat and Mass Transfer* 1972; **15**: 1787–1806.
4. Van Doormal JP, Raithby GD. Enhancement of the SIMPLE method for predicting incompressible fluid flows. *Numerical Heat Transfer* 1984; **7**: 147–163.
5. Markatos NC, Pericleous KK, Simitovic R. A hydrometeorological, three-dimensional model of thermal energy releases into environmental media. *International Journal for Numerical Methods in Fluids* 1987; **7**: 263–276.
6. Barakos G, Mitsoulis E, Assimacopoulos D. Natural convection flow in square cavity revised: laminar and turbulent models with wall functions. *International Journal for Numerical Methods in Fluids* 1994; **18**: 695–719.
7. Peric M. A finite volume method for the prediction of three-dimensional fluid flow in complex ducts. PhD Thesis, University of London, 1985.
8. Date AW. Solution of Navier–Stokes equations on non-staggered grid. *International Journal for Heat and Mass Transfer* 1993; **36**: 1913–1922.
9. Rhie CM, Chow WL. A numerical study of the turbulent flow past an isolated airfoil with trailing edge separation. *AIAA Journal* 1983; **21**: 1525–1532.
10. Majumdar S. Role of underrelaxation in momentum interpolation for calculation of flow with non-staggered grids. *Numerical Heat Transfer* 1988; **13**: 125–132.
11. Miller TF, Schmidt FW. Use of a pressure-weighted interpolation method for the solution of the incompressible Navier–Stokes equations on a non-staggered grid system. *Numerical Heat Transfer* 1988; **14**: 213–233.
12. Aksoy H, Chen C-J. Numerical solution of Navier–Stokes equations with non-staggered grids. *Numerical Heat Transfer B* 1992; **21**: 287–306.
13. Melaaen MC. Calculation of fluid flows with staggered and non-staggered curvilinear non-othogonal grids—the theory. *Numerical Heat Transfer B* 1992; **21**: 1–19.
14. Melaaen MC. Calculation of fluid flows with staggered and non-staggered curvilinear non-othogonal grids—a comparison. *Numerical Heat Transfer B* 1992; **21**: 21–39.
15. Choi SK, Yun Nam H, Cho M. Use of staggered and nonstagerred grid arrangements for incompressible flow calculations on nonorthogonal grids. *Numerical Heat Transfer B* 1994; **25**: 193–204.
16. Choi SK, Nam HY, Cho M. Systematic comparison of finite volume methods with staggered and non-staggered grid arrangements. *Numerical Heat Transfer B* 1994; **25**: 205–221.

17. Leonard BP. A stable accurate convective modelling procedure based on quadratic upstream interpolation. *Computational Methods in Applied Mechanical Engineering* 1979; **19**: 59–98.
18. Arampatzis G, Assimacopoulos D, Mitsoulis E. Treatment of numerical diffusion in strong convective flows. *International Journal for Numerical Methods in Fluids* 1994; **18**: 313–331.
19. Ghia U, Ghia KN, Shin CT. High-*Re* solutions for incompressible flow using the Navier–Stokes equations and a multigrid method. *Journal of Computational Physics* 1982; **48**: 387–411.
20. Stone HL. Iterative solution of implicit approximation of multidimensional partial differential equations. *SIAM Journal of Numerical Analysis* 1968; **5**: 530–558.